Investigating cyclopentane hydrate nucleation and growth using microfluidics

Peyman Dehghani, Anne Sinquin, Nicolas Gland, Anh Minh Tang, Audrey Estublier

▶ To cite this version:

Peyman Dehghani, Anne Sinquin, Nicolas Gland, Anh Minh Tang, Audrey Estublier. Investigating cyclopentane hydrate nucleation and growth using microfluidics. Science and Technology for Energy Transition, 2023, 78, pp.36. 10.2516/stet/2023034 . hal-04372811

HAL Id: hal-04372811

https://ifp.hal.science/hal-04372811v1

Submitted on 4 Jan 2024

Science and Technology for Energy Transition **78**, 36 (2023)
© The Author(s), published by EDP Sciences, 2023
https://doi.org/10.2516/stet/2023034

Selected Papers from First European Conference on Gas Hydrates (ECGH), 2022
Bertrand Chazallon and Anh Minh Tang (Guest Editors)

Available online at:
stet-review.org

REGULAR ARTICLE OPEN ACCESS

Investigating cyclopentane hydrate nucleation and growth using microfluidics

Peyman Dehghani[1], Anne Sinquin[1,*], Nicolas Gland[1], Anh Minh Tang[2], and Audrey Estublier[1]

[1] IFP Energies nouvelles, 1-4 Avenue de Bois-Préau, 92852 Rueil-Malmaison, France
[2] Navier, Ecole des Ponts, Université Gustave Eiffel, CNRS, Marne-la-Vallée, France

Received: 11 May 2023 / Accepted: 6 November 2023

Abstract. The success of geological storage of carbon dioxide (CO_2) in depleted oil and gas reservoirs relies among other aspects on the efficiency of CO_2 injection, especially in the near-wellbore area where flow rates are high. CO_2 hydrates pressure/temperature equilibrium conditions may be reached in this zone due to cooling associated with the Joule–Thomson effect; such CO_2 hydrate formation may lead to strong injectivity loss and impair drastically the onsite well operations. In this study, cyclopentane hydrates (CPH) were employed as CO_2 hydrate proxy (*i.e.* formation at atmospheric pressure) to mimic CO_2 hydrate formation at higher pressure. In this study, the nucleation and growth processes were determined using a droplet-based in-house-microfluidic device. The generation of water droplets in cyclopentane liquid using the co-flow method was achieved. Trains of identical water droplets were stored in a serpentine channel. Each isolated droplet in this channel serves as a separate reactor. The temperature was controlled using a Peltier module to initiate hydrate nucleation at low temperatures. The isolated droplets provided the opportunity to statistically analyze the kinetic behaviors by varying key parameters, such as thermal history and water salinity. Detection of the onset of crystallization in water droplets over time and temperature allowed us to plot conversion curves based on imposed parameters. The effect of thermal history and dissociation temperature was first compared using pure water. This study marks the initial investigation into how NaCl influences CPH formation in microfluidic devices, focusing on isolated water droplets within serpentine tubes. The progression of ice nucleation, ice melting, the onset of CPH crystallization, CPH growth, and CPH dissociation are illustrated in water droplets exposed to changing temperatures. The addition of NaCl in the water during the procedure exhibited a noteworthy impact on CPH formations. With the same temperature profile, salt concentration delays nucleation (thermodynamic effect) and slows down growth. Our findings suggest that higher subcooling accelerates nucleation and growth rates. Initial lateral growth rates ranged from 4.22 μm/s to 2.14 μm/s, with a subcooling of 4.2 °C observed between 2 and 7 min for a pure water droplet.

Keywords: Cyclopentane hydrates, Nucleation, Crystallization kinetics, Microfluidic device, Salinity effect, CO_2 storage, Depleted reservoir.

1 Introduction

The success of the Paris Agreement could signify a crucial turning point for carbon capture and storage (CCS) [1]. CCS is a technology that aims to capture carbon dioxide (CO_2) emissions from power plants, industrial processes, and other sources and store them in underground reservoirs. The injection of CO_2 into a reservoir involves high CO_2 injection rates in the near well bore area of depleted oil or gas fields, or deep saline aquifers [2–4]. CO_2 is injected under pressure and is typically stored in a liquid or supercritical state in saline aquifers [3]. In depleted reservoirs, the pressure is low and the temperature is cold, these initial conditions coupled with the thermodynamic aspects of flow in the well and perforations (Joule–Thomson effect) bring potentially the system in the CO_2 hydrates zone stability [5, 6]. The formation of CO_2 hydrates at the beginning of CO_2 injection can lead to partial to complete clogging of porous rock formations where the pressure and temperature conditions are favorable for their formation [7, 8]. CO_2 hydrates will thus reduce the injectivity and to some extent the storage capacity of the reservoir which can pose a big challenge for carbon storage.

---

* Corresponding author: `anne.sinquin@ifpen.fr`

CO_2 hydrates are clathrate hydrates which are non-stoichiometric crystalline compounds. They consist of hydrogen-bonded water (host) molecules forming a crystalline lattice, which is stabilized by the presence of a hydrate-former (guest) in some of its cavities [7]. Guest molecules gas hydrates can include small gas molecules such as CO_2, H_2, CH_4, and N_2, as well as larger molecules like cyclopentane (CP) and tetrahydrofuran (THF) [8]. Hydrates form typically under low temperatures (negative to a few degrees above 0 °C) and high pressures (some bar to several hundred bar). In CCS as well as in various industrial applications such as gas storage and water desalination technologies, hydrates can potentially be formed in porous rocks that are partially to fully saturated with water.

Molecules such as THF and CP form hydrates under atmospheric pressure. They form SII hydrate structures at temperatures below 3.85 and 7.2 °C, respectively [9–11]. A difference between these two compounds is that THF is completely soluble in water, while CP has low solubility in water (0.156 g/L at 25 °C) [12]. Research on cyclopentane hydrate (CPH) has focused on understanding their formation and properties, as well as their potential applications in various industries such as gas storage and water desalination. Many studies have been conducted on the formation, dissociation, and phase equilibrium of CPH. Most of them have been done in large reactors [12–15]. These studies have provided information on the effects of temperature, pressure, and water salinity on CPH formation and dissociation.

Despite their potential to provide direct visual observations at the scale of pores in host rocks (below hundred microns), the study of CPH by microfluidic is relatively new. A few studies on CPH using microfluidics have recently been reported. These studies have been conducted using industrial microfluidic devices [16], or in-house-millifluidic devices [11]. Microfluidic is a technology that deals with the manipulation of small fluid volumes within a confined space, usually on the microliter or nanoliter scale. This technology is used for many experiments such as droplet generation (T-junction, flow focusing, co-flow), mixing, or separation [17]. Microfluidic allows precise control of fluid flow rate, temperature, and pressure, which are important parameters to study the formation of clathrate hydrates [17, 18]. Atig *et al.* [19] introduced a method for studying crystal nucleation under controlled pressure, and melting processes by observing a single drop. The experiments were conducted using CP, a hydrate-former, as the carrier oil, and dissolved CO_2, also a hydrate-former and a "help gas" for CPH formation. In another work, Touil *et al.* [20] developed an experimental method to study the crystallization and growth of gas hydrates in thin glass capillaries. This work was conducted under a range of supercooling conditions for CO_2 in liquid and gaseous form. This setup allows for detailed microscopic observations of the impact of supercooling and substrate wettability on hydrate growth and their interaction with the substrate. Therefore, it is essential to directly explore the formation mechanisms of CPH. Li *et al.* [16] observed the dissociation behavior of CPH in a commercial microfluidic device, and the effects of salt and surfactant on hydrate dissociation were considered.

Injection and storage of CO_2 in deep saline aquifers or depleted reservoirs require an understanding of the effect of salts (composition and amount) on hydrate formation. Many experimental studies have been reported in bulk (typically a few hundreds of mL). Cai *et al.* [21] followed the kinetics of the formation of CP-methane hydrates in a 450 mL stainless steel reactor by measuring the evolution of temperature and pressure phase equilibrium conditions at three salinity levels (0, 3.5%, and 7.0% (w/w) in NaCl) and within the pressure range of 1–3 MPa. Martinez de Baños *et al.* [11] visualized the kinetics of CPH crystallization in an in-house millifluidic device, and examined subcooling required for different dissociation temperatures of primary CPH and then they plotted conversion curves (secondary CPH formation) as a function of subcooling to study the effect of water salinity with a concentration of 5 g/L [0.1 M NaCl].

The onset of hydrate formation is a stochastic phenomenon and nucleation elementary process is very difficult to catch and study. The stochastic character of this process requires a statistical approach with many data. As a consequence, there's a strong interest to using microfluidic devices and performing simultaneous tests on multiple samples (each droplet is considered an isolated system) on a micro or nano-liter scale. In this experimental study, CPH was studied to provide a statistical view of the CPH nucleation at the pore scale. Data on the hydrate growth rate will also be given at this scale. An in-house droplet-based microfluidic device was designed and built to study the nucleation and growth processes of hydrates. This setup allowed for the simultaneous observation of CPH formation in approximately 60 droplets under constant temperature conditions. This large number of droplets (where each isolated droplet in this channel serves as a separate reactor) provided the opportunity for minimizing repetitive experimental durations and also statistical analysis of kinetic behaviors by varying parameters such as thermal history and salinity. The conversion curves were plotted based on the onset of crystallization in water droplets over time and subcooling. The impact of thermal history was first compared using pure water. The effect of water salinity (NaCl brine) on the onset of CPH formation was then investigated by testing four different salt concentrations: 5 g/L, 17.5 g/L, 23.4 g/L and 32 g/L.

2 Experimental method

2.1 Development of the experimental setup

Figure 1 illustrates a schematic of the developed experimental setup. Two syringe pumps (a) were employed to inject water and CP simultaneously, producing identical droplets stored in a serpentine tube with a specified distance apart (b–d). The temperature of the storage section was regulated using a power source and thermostatic bath to control the cold side of the Peltier module (e–g). The formation of CPH was observed by a microscope and recorded by a high-speed camera (h, i). Videos and images were saved on a computer (j). The details of the setup are described below.

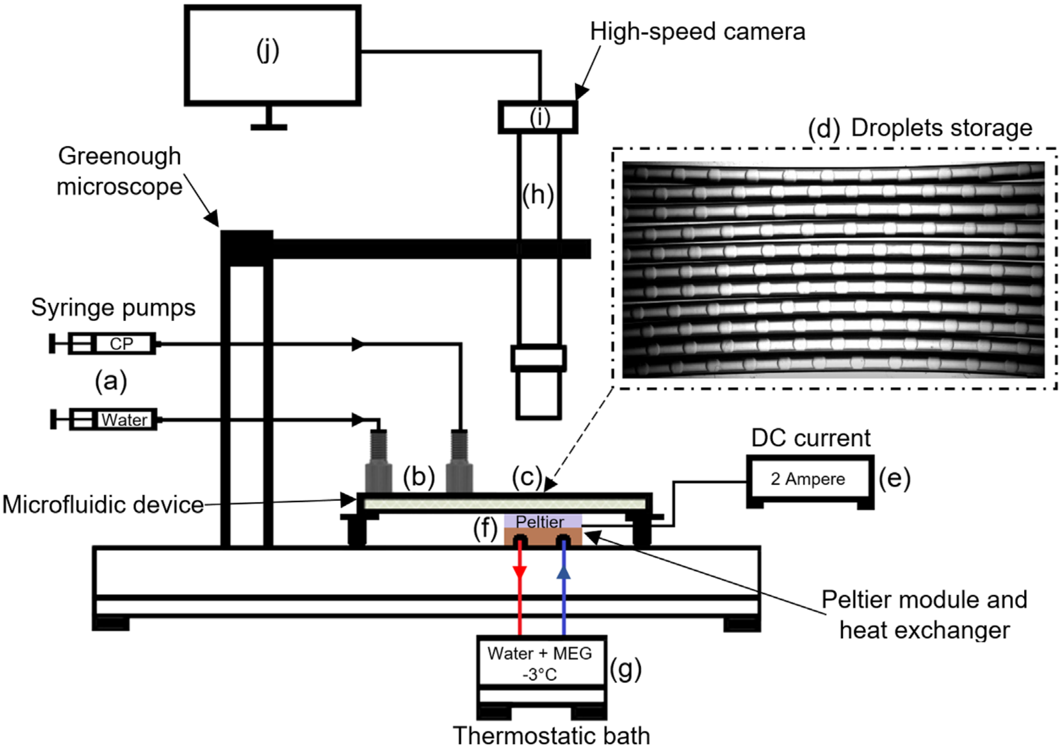

Figure 1. Experimental setup: (a) syringe pumps, (b) microfluidic design-droplets generation, (c) microfluidic design-droplets storage, (d) Overview of the serpentine tubes containing the immobile water/CP, (e) power supply, (f) Peltier module + heat exchanger, (g) thermostatic bath, (h) Greenough stereo microscope, (i) high-speed camera and (j) data and image acquisition system.

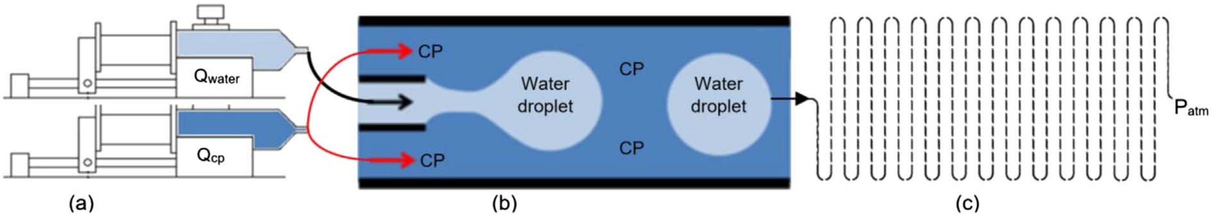

Figure 2. Schematic of the microfluidic system: (a) syringe pumps, (b) schematic of droplet formation by co-flow geometry in the dripping regime, the tapered inner capillary in the outer capillary and (c) layout of a microfluidic device with serpentine channel.

To develop the experimental setup, several key steps were considered:

1. A microfluidic droplet generator was required to produce reproducible small water droplets, ranging in diameter from 700 µm to 900 µm (Fig. 2b). The droplet size must be maintained the same for all droplets in the channels and should be adjustable for each test.
2. A capillary tube was required to generate water droplets within an oil flow (water-in-oil) or on a hydrophobic surface. The fluid behavior is significantly impacted by the hydrophilic or hydrophobic nature of the inner surface of the microchannel. If the surface is hydrophilic, the production of reproducible small water droplets in CP will not be possible [19, 22].
3. The generated droplets must be directed towards the droplet storage section, which should feature a compact design to allow optimal placement under a microscope and accommodate a maximum number of serpentine tubes. This will ensure efficient utilization of limited space, with a capacity ranging from 150 to 200 water droplets stored in a space of 40 × 40 mm (Fig. 2c).
4. The type of droplet storage tube should be chosen based on specific system requirements, such as transparency for imaging under a microscope, compatibility between the injected phases (CP and water), and ability to form a spiral or a serpentine configuration within the droplet storage section.
5. The microfluidic system should be designed to integrate into other devices, such as syringe pumps for injecting two-phase liquids and a temperature control system capable of rapidly, efficiently, and adjustably cooling the droplet storage section (Fig. 2a).

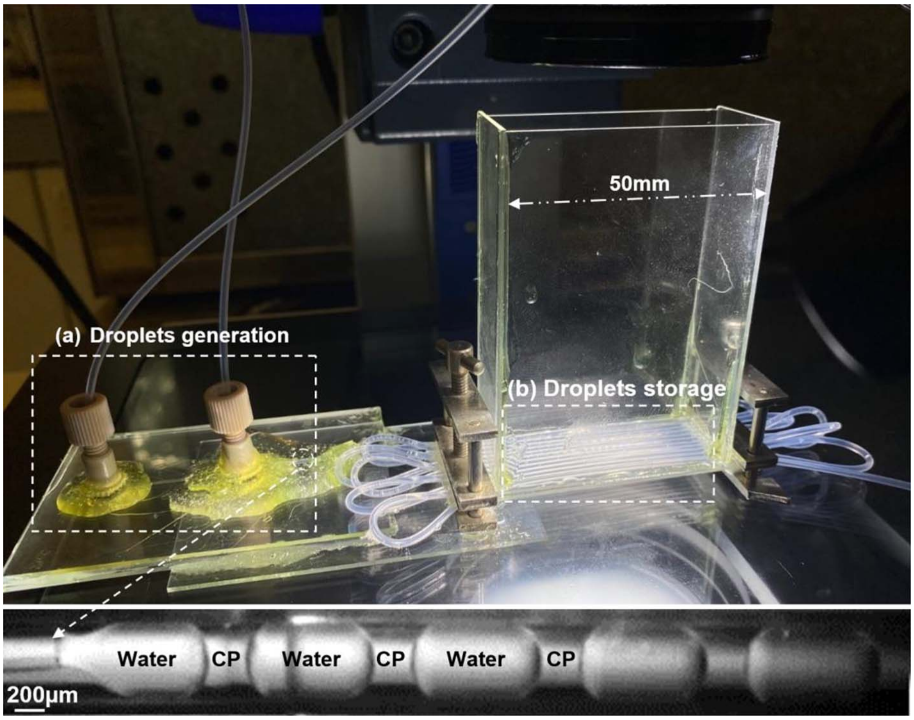

Figure 3. Photograph of the microfluidic chip, (a) microfluidic design-droplets generation with a view of the co-flow injection in the dripping regime and (b) droplets storage section.

2.1.1 Droplets generation

The co-flow method was used to generate monodisperse water droplets by flowing a continuous phase of CP and a dispersed phase of water in the same direction (Figs. 2b–3a). In co-flow geometry, the dispersed and continuous phase fluids meet in parallel streams. The microfluidic chip consists of a round external hydrophobic perfluoroalcoxy-alcane (PFA) tube, (outer diameter of 1.59 mm and inner diameter of 0.75 mm) and a square internal capillary glass (inner section of 0.2 × 0.2 mm). The square capillary glass was connected to the first nano-port to dispense the water phase. The round PFA tube was used for the continuous phase of CP injection.

To produce uniform droplets, the flow rate of the continuous phase must be consistent on both sides of the inner tube. To achieve this, the inner tube was chosen to be square and placed at the center of the PFA round tube. Two syringe pumps were used to inject water through the first nano-port and CP through the second nanoport. Two ring gaskets were utilized to seal the nano-ports on the microscope slide, and then they were affixed to the glass substrate using epoxy glue.

2.1.2 Droplets storage

According to the dimensions of the Peltier module, a serpentine form must be created to maximize the number of tubes in a small space. Two adjustable metal clamps were fixed onto the second glass (Fig. 3b). The droplet generation tube PFA was passed through these clamps to create a serpentine form between the two metal clamps. In this section, there are nine PFA tubes providing 360 mm of observation length (*i.e.* 9 meanders of 40 mm) (see Supplementary Information Video 1 for an overview of the serpentine tubes and the generation of identical water droplets by maintaining equal cyclopentane volume between the droplets). The tubes were then assembled parallel to each other, stretched on both sides and securely fixed to a glass surface to have a homogeneous temperature in all of the tubes. A small glass pool was created around the droplet storage, it will be described in the next section.

2.1.3 Temperature control and measurement

A Peltier module (TEC1-12706) with dimensions of 40 × 40 × 3.6 mm was used to control the temperature of the droplet storage. A power supply (EL302T, Triple Output, 2×30V/2A+5V/1A) was employed to provide the necessary voltage and current for the thermoelectric effect of the Peltier module. A heat exchanger made of pure copper with dimensions of 40 × 40 × 10 mm was used to cool the hot side of the Peltier module. A wired digital thermometer (RS PRO RS55-II, with an accuracy of ±0.7 K) was integrated to measure the temperature of the droplet storage.

The top section of the Peltier module (cold face) was placed in direct contact with the microchip droplets storage, and the bottom section (hot face) was placed on a heat exchanger for cooling, as shown in Figure 4. The hot face must be cooled as much as possible to achieve very low temperatures.

A heat exchanger made of pure copper, which functions as a cooling water block, was used (Fig. 4). The internal

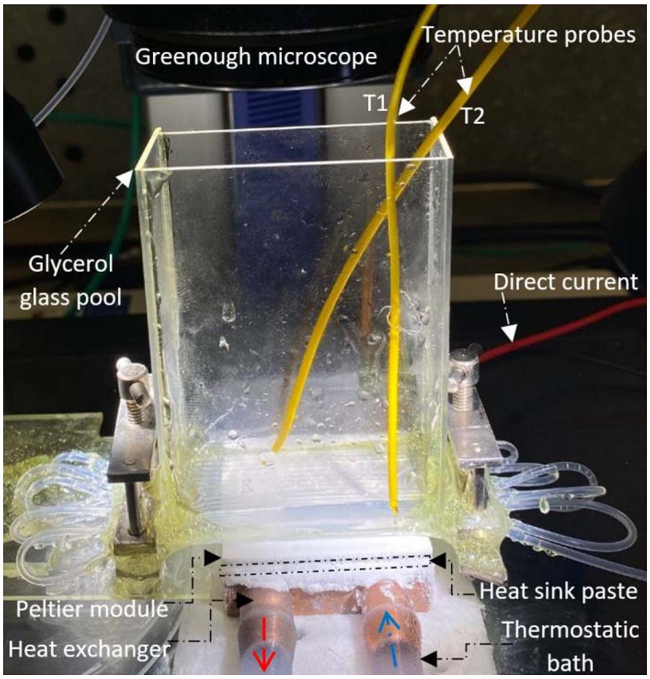

Figure 4. Design of temperature control and measurement.

flow channel, which was connected to a thermostatic bath, has a diameter of 6 mm and a double U-shaped design. The heat generated on the hot side of the Peltier device was evacuated through a cooling circuit that circulates a mixture of water and glycol (60% water, 40% glycol) at a temperature of –3 °C. This temperature was set based on the cold face temperature (T_c) required (–25 °C) and considering the thermal gradient of the Peltier module ($\Delta T = 70$ °C) corresponding to the difference between the temperature of the hot and the cold faces ($\Delta T = T_h - T_c$). Additionally, two insulating jackets were placed around the input and output tubes between the heat exchanger and the thermostatic bath to minimize frigories loss [23, 24]. A layer of silicon heat sink paste (5 W/(m·K)) was placed between the heat exchanger and the hot face of the Peltier to enhance thermal conductivity (Fig. 4).

A direct current was applied to the Peltier module, which transferred heat from one side to the other. By adjusting the current applied to the module (in this case, 2A), the temperature of the droplet storage can be decreased to –35 °C.

A small glass pool was created around the droplet storage to enable the injection of glycerol into it (Fig. 4). This method allowed maintaining the image quality by the camera at low temperature. Glycerol has high transparency and it covers the serpentine tube up to a height of 2–3 mm, preventing the formation of dews on the cold tube surface. It also helps to homogenize the temperature in the pool. A wired digital thermometer was integrated for temperature measurement within the microchip droplet storage pool allowing for precise control of differential temperature between probes 1 and 2, $T1$ and $T2$, respectively (Fig. 4).

2.2 Experimental procedure

Deionized water (here as pure water) with a resistivity of 18.2 mΩ/cm was prepared using Milli-Q (IQ-7000) and CP (HPLC grade) was supplied by Alfa Aesar. To investigate the effect of water salinity, four NaCl solutions (NaCl provided by *Fisher Scientific*, purity 99.5%) were prepared at the following concentrations: 5 g/L [0.1 M], 17.5 g/L [0.3 M], 23.4 g/L [0.4 M] and 32 g/L [0.55 M].

The procedure consists of three crystallizations (ice then two CPH formations). Ice was first formed and then melted by heating at a temperature slightly above 0 °C. This melting initiates the first CPH formation. In practice, nucleation can occur spontaneously (homogeneous nucleation) or be induced by impurities (heterogeneous nucleation) or residual crystal networks due to recent hydrate dissociation (secondary nucleation) [25–27]. The formation of hydrates in static systems is difficult and can take an extremely long time, even with intense subcooling [28]. Afterward, CPH is dissociated and the system is brought once again into the hydrate stability zone for the second CPH formation. This procedure can shorten the induction time, particularly in cases of crystallization without agitation in very small reactors or in microfluidic systems [11].

2.2.1 Test procedure

Figure 5 displays the temperature of the droplet storage section (measured by the digital thermometer) *versus* the elapsed time corresponding to this procedure which includes four steps:

1. temperature is decreased from the ambient one to −25 °C to convert the liquid water droplets into ice;
2. temperature is increased from −25 °C to 7.2 °C in two stages: (i) from −25 °C to 0 °C at a heating rate of 5 °C/min and (ii) from 0 °C to 7.2 °C at a heating rate of 0.5 °C/min. The primary CPH formation can occur during the second stage;
3. temperature is maintained at a dissociation value (T_{dis}) higher than the equilibrium temperature ($T_{eq} = 7.2$ °C) during an exposure time (t_{dis}) to dissociate primary CPH;
4. temperature is decreased from T_{dis} to 0 °C at a cooling rate of 0.5 °C/min to initiate the secondary CPH formation. The high-speed camera recorded the onset of the secondary CPH formation during this step.

2.2.2 Test program

Table 1 presents the test program, it consists of two parts. The parameters associated with each test are illustrated in Figure 5. The first part includes Tests A1–A5, which were conducted from 0 g/L (A1 and A2) to 32 g/L (A5) with varying concentrations of NaCl. The second part includes Tests 1–8, which were performed to investigate the onset of secondary CPH formation. Tests 1–4 were performed with pure water. In these conditions, the equilibrium temperature of CPH hydrates dissociation is 7.2 °C [11]. To

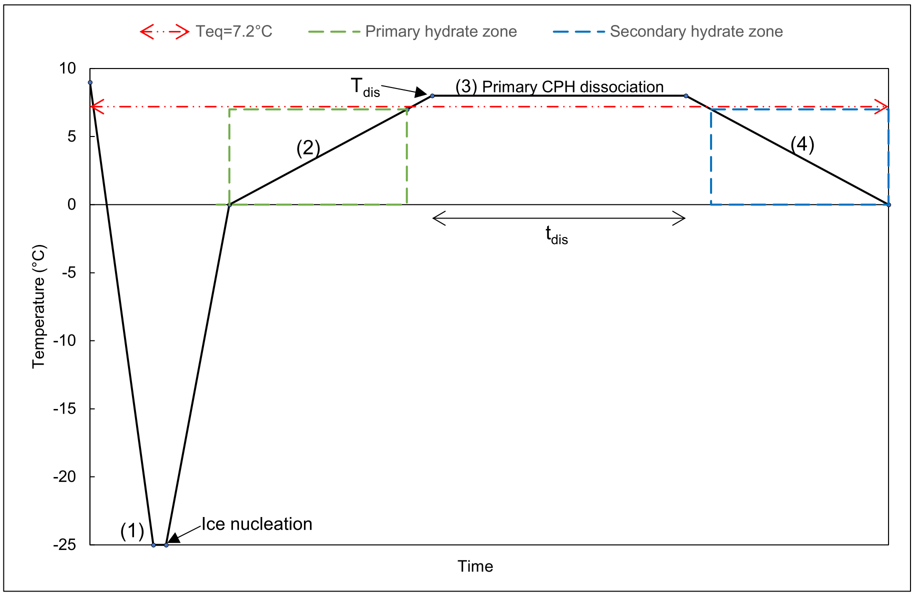

Figure 5. Sequence of temperature variations (1) ice nucleation, (2) primary hydrate zone, (3) primary CPH dissociation and (4) secondary hydrate zone.

Table 1. Test program.

Type of test	Test number	Salinity NaCl (g/L)	T_{eq} (°C)	T_{dis} (°C)	t_{dis} (min)	T_{max} (°C)	Number of droplets produced
Ice nucleation	A1	0	–	–	–	−25	41
	A2	0	–	–	–	−25	44
	A3	5	–	–	–	−25	17
	A4	17.5	–	–	–	−25	17
	A5	32	–	–	–	−25	17
Onset of secondary CPH formation	1	0	7.2	7.5	90	–	39
	2	0	7.2	8.3	90	–	34
	3	0	7.2	8.8	20	–	39
	4	0	7.2	8.8	90	–	50
	5	5	7.1	7.5	20	–	17
	6	17.5	6.4	7.5	20	–	17
	7	23.4	6.2	7.5	20	–	56
	8	32	5.9	7.5	20	–	17

dissociate CPH the temperature plateau applied to dissociated the CPH crystals must be higher than this value. T_{dis} for Tests 1 and 2 have been set at 7.5 °C and 8.3 °C, respectively (with a duration of dissociation $t_{dis} = 90$ min). Similarly, for Tests 3 and 4, dissociation durations of 20 min and 90 min, respectively, were applied at a temperature $T_{dis} = 8.8$ °C.

The salts are thermodynamic inhibitors like alcohols. Consequently increasing the salt concentration in the water leads to displacing the equilibrium temperature towards a lower temperature. Tests 5–8 involved an incremental increase of the salinity, resulting in a shift of the equilibrium dissociation temperature to 7.1 °C, 6.4 °C, 6.2 °C and 5.9 °C [29], respectively for 5, 17.5, 23.4 and 32 g/L NaCl. For all four salinity tests, the dissociation temperature and dissociation time were set at 7.5 °C and 20 min. The droplet size (length) for all of the tests was 875 ± 25 μm. Given that the microfluidic device has the capacity to store between 150 and 200 water droplets, depending on their size and spacing, it was necessary to limit the number of droplets (60 droplets) for manual image analysis, as no automated method was utilized. This approach enabled the completion of image analysis within shorter time intervals. Also, to ensure maximum accuracy of manual image analysis for salt tests, the number of droplets was significantly reduced (compared to the capacity of the device).

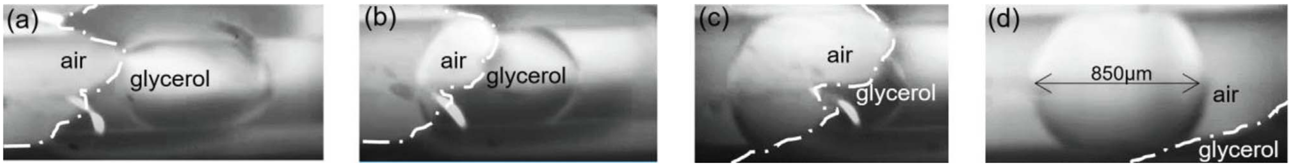

Figure 6. The distinct forms and diameter size of droplets under conditions of air *versus* glycerol with refractive index equals 1 and 1.47, respectively, (a) the Teflon tube containing a water droplet fully immersed in glycerol, (b, c) Teflon tube half immersed in glycerol and the other part in contact with air, (d) Teflon tube entirely in air.

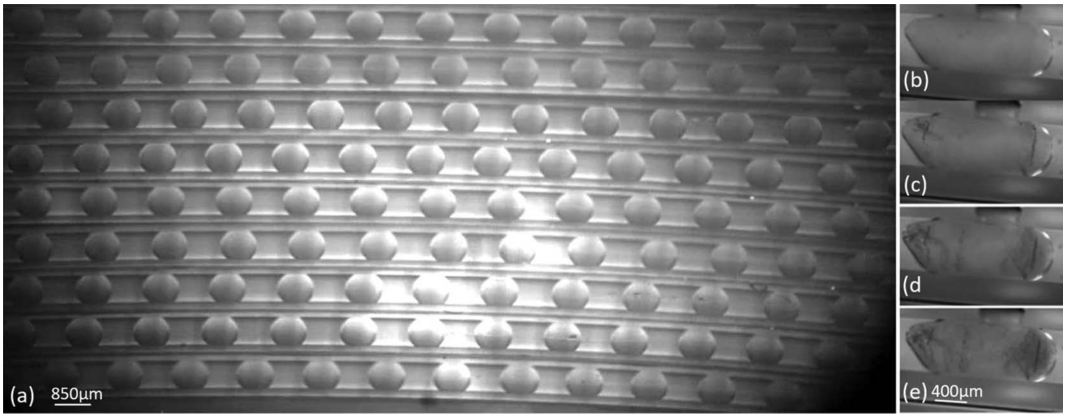

Figure 7. (a) Storage of the pure water droplets in an empty bath at ambient temperature, (b–e) snapshots of ice nucleation in the glycerol bath.

2.3 Image analysis

Optical components, including binocular vision, a high-speed camera, and light sources, were used to visualize the droplets moving through the microfluidic chip. A Greenough stereo microscope (ZEISS STEMI 508) with an 8:1 zoom range (0.63× to 5×) was employed to observe all the serpentine tubes at magnifications of 1× or 2×. This microscope was connected to a high-speed camera (*i*-speed 230) with a maximum frame rate of 225,000 fps to capture magnified images of the water droplets. A light source (CL4500 LED CRI90) with a maximum light flux of 450 lm was used to provide illumination for the optical components.

The onset of secondary CPH formation in a single water droplet was detected when the hydrate crystals became visible within the resolution of the optical setup. The formation of hydrates occurs in two steps: (i) nucleation, which is a microscopic and stochastic phenomenon: small nuclei appear in the droplets; (ii) and crystal growth process, which occurs when nuclei reach a critical size [28]. It was assumed that the statistical behavior of both steps is similar [11].

It is worth emphasizing that the refractive index of the pool glass was altered upon the injection of glycerol. This phenomenon is illustrated in Figure 6, which demonstrates the distinct forms of droplets under conditions of air (refractive index = 1) *versus* glycerol (refractive index = 1.47) as the medium through which light passes.

3 Results

3.1 Ice nucleation

According to Figure 5, the ambient temperature was decreased to −25 °C to convert the water droplets from liquid to ice. During this step, after the production of stationary pure water droplets (Fig. 7a), the moment when ice nucleation was observed (Fig. 7e) was considered as the point of ice nucleation and used to determine the number of transformed droplets *versus* time. It should be noted that this event happens very fast and the duration between Figures 7b and 7e was in a range of milliseconds. However, when salt was added, the detection of this event was different compared to pure water.

Figures 8 and 9 illustrate graphically the ice nucleation of respectively pure water droplets and saltwater droplets. Figure 8 presents the percentage of pure water droplets turned to ice for each minute for the Tests A1 and A2 performed in the same conditions. The total number of droplets in these two tests was 41 and 44 for Tests A1 and A2, respectively. During the first minute, no droplet was turned into ice. During the second minute, only 2% of droplets in Test A1 were turned into ice. The maximum droplets were turned to ice during the 4th minute. It represents the main peak in this histogram (about 40% of droplets). Although the decline is not precisely the same in both histograms, the water-to-ice droplet conversion exhibits a decreasing trend within the next few minutes.

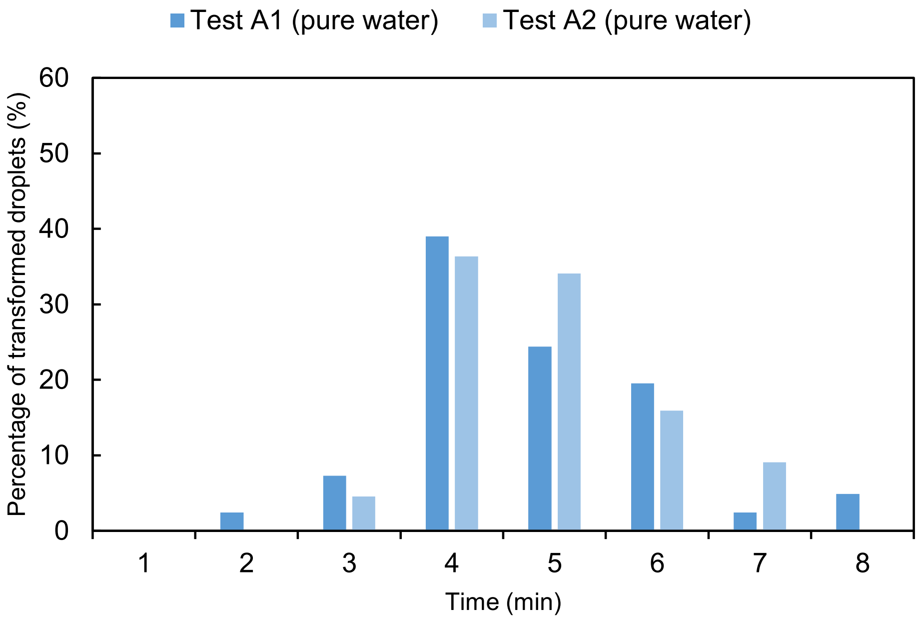

Figure 8. Ice nucleation in Tests A1 and A2: percentage of pure water droplets transformed into ice during each minute.

During the 5th minute, 24% and 34% of the droplets turned into ice for Tests A1 and A2, respectively. A small percentage of these droplets turned into ice during the last two minutes (7th and 8th minutes).

Figure 9 presents the percentage of salted water droplets that turned into ice for three concentrations of NaCl *versus* time. The main peak, representing 50% of droplets crystallized was reached during the 4th minute for 5 g/L NaCl (Test A3). For the concentrations of 17.5 g/L (Test A4) and 32 g/L (Test A5) NaCl, the main peaks were reached during the 5th minute with respectively 47% and 41% of droplets transformed. At 32 g/L NaCl (Test A5) the droplets took a longer time to transform into ice. Respectively 10% and 6% of the droplets formed ice during the 7th and 8th minutes.

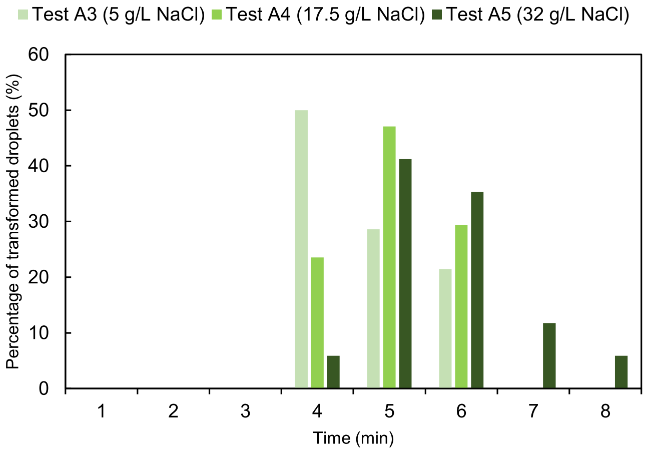

Figure 9. Ice nucleation in Tests A3–A5, percentage salt water droplets transformed into ice during each minute.

3.2 Primary CPH formation

The purpose of this experiment was to improve our understanding of the CPH crystallization phenomenon with the different elementary processes (hydrate's nucleation and growth) and of the CPH dissociation. A first test was performed to observe precisely these hydrates crystallization/dissociation processes on a single water droplet. Figure 10 depicts the primary formation and dissociation of CPH for a pure water droplet at various temperatures. The illustration provides an overview of the correlation between the progression of the primary CPH formation phases in a water droplet. The process was conducted by first decreasing the temperature to −25 °C and then increasing it above 0 °C to initiate the CPH first formation.

Step (a) displays a water motionless droplet of pure water at ambient temperature. Steps (b–d) show temperature reduction to −25 °C: the water droplet turns into ice at −17 °C. Step (e) illustrates the ice melting (possibly with hydrate) at +1 °C. Upon passing this ice melting step, the onset of hydrate crystallization (primary CPH formation) is apparent at 3 °C (f) and the crystal growth continues until the system reaches the CPH equilibrium temperature, $T_{\text{eq}} = 7.2$ °C (g–i). After passing this equilibrium temperature (j), hydrate dissociation begins slowly and as the temperature increases the crystal structure disappears quickly (k). As long as the increase in temperature rate is not negligible, the temperature corresponding to crystal disappearance is measured above the CPH equilibrium of dissociation ($T_{\text{dis}} = 7.2$ °C) (j, k).

3.3 Onset of secondary CPH formation

Figures 11a–11e depicts the progression of crystallization in one pure water droplet as an example. In Figure 11b the onset of crystallization is localized with an arrow. This

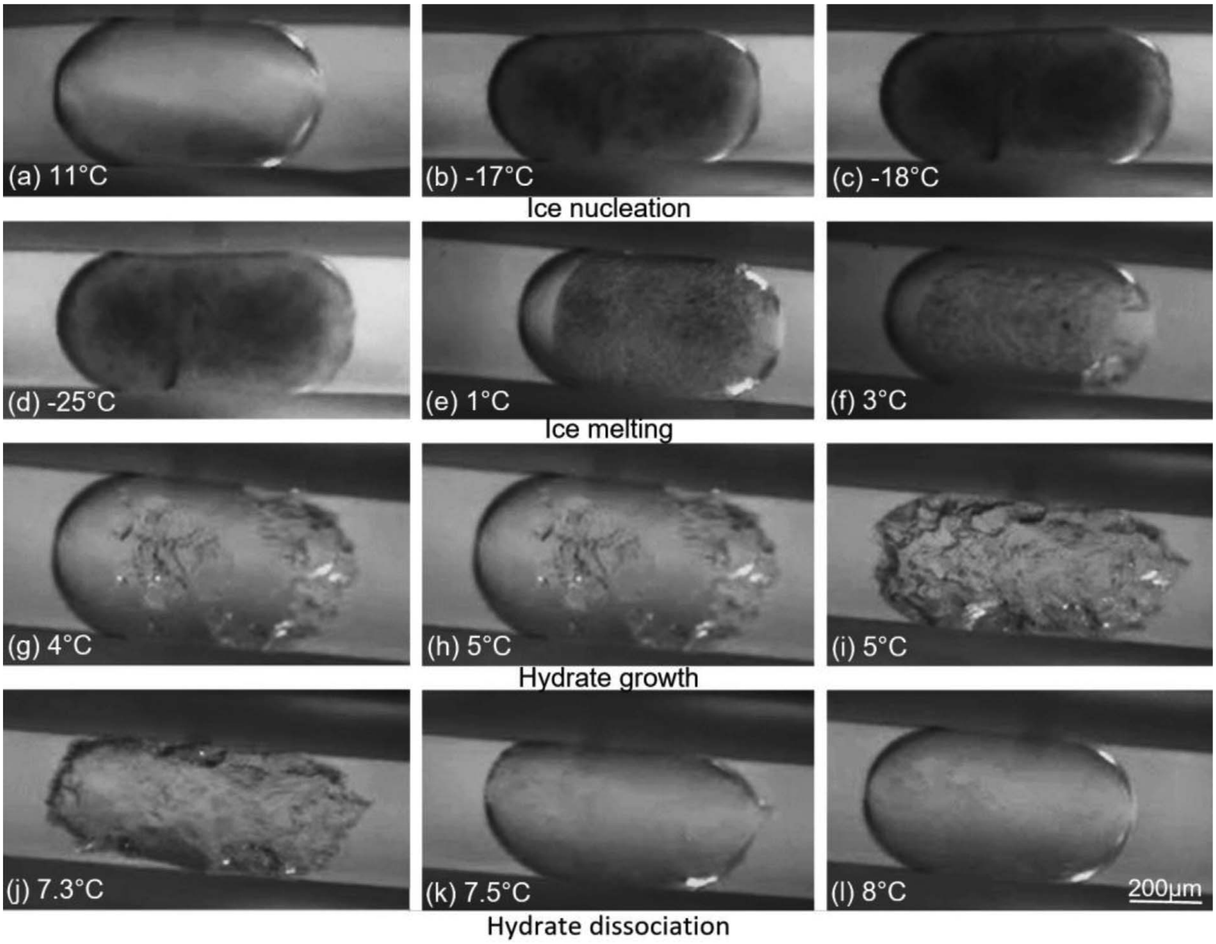

Figure 10. Snapshots of a pure water droplet *versus* temperature. (a) Initial liquid water droplet, (b–d) ice nucleation, (e, f) ice melting and onset of primary CPH crystallization, (g–i) CPH growth, (j, k) CPH dissociation and (l) final liquid water droplet.

Figure 11. Example of progression of CPH crystallization in a pure water droplet – secondary CPH formation.

event was detected in all the droplets as a function of the subcooling applied for all tests. The influence of temperature of dissociation (T_{dis}) and of the dissociation duration (t_{dis}) on the formation of the secondary CPH were explored in this study. Four tests were conducted to dissociate the primary CPH with pure water at various T_{dis} and t_{dis} (Tests 1–4, see Tab. 1). The secondary formation was achieved in the same conditions for these tests where the temperature was lowered at an identical rate (0.5 °C/min). The final temperature was set slightly above 0 °C. The results are plotted in Figures 12–15.

The CPH nucleation results for two melting conditions of the primary CPH, T_{dis} equals to 7.5 °C (Test 1) and 8.3 °C (Test 2) with the same dissociation duration of t_{dis} = 90 min, are presented in Figure 12 where the conversion fraction is presented as a function of the subcooling $\Delta T = T_{\text{eq}} - T_{\text{exp}}$. The conversion fraction is defined as the percentage of droplets transformed into CPH. Note that the subcooling is related to the driving force for the crystallization and is defined as the difference between the experimental temperature (T_{exp}, which is the temperature of the droplets storage measured by the digital thermometer) and the equilibrium temperature (T_{eq}) [30]. For pure water, T_{eq} was 7.2 °C [13]. The results of Test 1 (T_{dis} = 7.5 °C) show that the onset of crystallization was detected on all droplets within subcooling of 3.1–4.2 °C. For Test 2 (T_{dis} = 8.3 °C), CPH crystallization was not observed in all the droplets. The conversion fraction reached 79% within a subcooling of 7.2 °C. Test 4 (T_{dis} = 8.8 °C) shows that the onset of crystallization was detected within

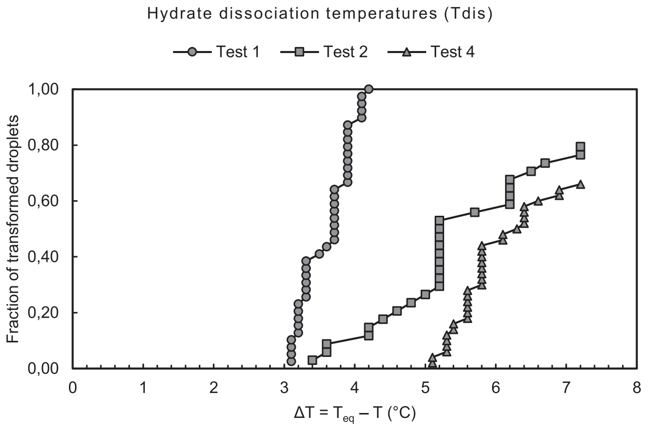

Figure 12. Secondary CPH nucleation of Tests 1 (pure water), Test 2 (pure water) and Test 4 (pure water): conversion fraction *versus* subcooling $\Delta T = T_{\mathrm{eq}} - T_{\mathrm{exp}}$ with various hydrate dissociation temperatures (T_{dis} of the primary CPH, dissociation duration $t_{\mathrm{dis}} = 90$ min).

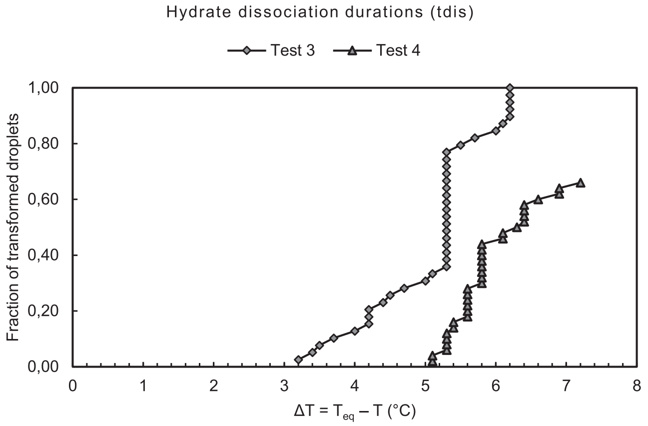

Figure 13. Secondary CPH nucleation Tests 3 (pure water) and 4 (pure water): conversion fraction *versus* subcooling $\Delta T = T_{\mathrm{eq}} - T_{\mathrm{exp}}$, with various dissociation durations (t_{dis}), hydrate dissociation temperature of the primary CPH $T_{\mathrm{dis}} =$ 8.8 °C.

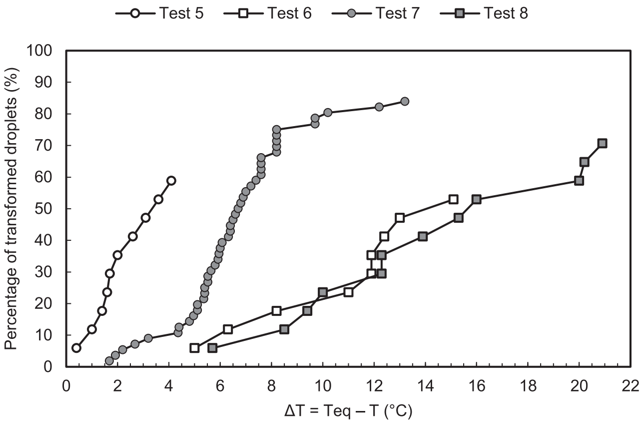

Figure 14. Secondary CPH nucleation Test 5 (5 g/L NaCl), Test 6 (17.5 g/L NaCl), Test 7 (23.4 g/L NaCl) and Test 8 (32 g/L NaCl): conversion fraction *versus* subcooling $\Delta T = T_{\mathrm{eq}} - T_{\mathrm{exp}}$, with dissociation durations ($t_{\mathrm{dis}} = 20$ min), hydrate dissociation temperature of the primary CPH $T_{\mathrm{dis}} =$ 8.8 °C.

subcoolings of 5.1–7.2 °C and the conversion fraction reached 66%.

Figure 13 displays the results of CPH secondary hydrate nucleation for two different dissociation durations $t_{\mathrm{dis}} = 20$ min (Test 3) and $t_{\mathrm{dis}} = 90$ min (Test 4) at an identical temperature of dissociation $T_{\mathrm{dis}} =$ 8.8 °C. The onset of crystallization for all isolated droplets at $t_{\mathrm{dis}} = 20$ min (Test 3) was observed between subcooling of 3.2 °C and 6.2 °C. With $t_{\mathrm{dis}} = 90$ min (Test 4), only 66% of the droplets were able to initiate crystallization between subcooling of 5.1 °C and 7.2 °C.

Figure 14 depicts the onset of crystallization at various NaCl concentrations. In Tests 5–8, the equilibrium dissociation temperature (T_{eq}) was considered to be 7.1 °C, 6.4 °C, 6.2 °C, and 5.9 °C, respectively. At NaCl 5 g/L (Test 5), the crystallization onset occurs within the subcooling range of 0.4–4.1 °C. At the concentration of NaCl of 17.5 g/L (Test 6) hydrate onset was detected on a much broader range of subcooling from 5 °C to 15.1 °C. In the presence of a NaCl concentration of 23.4 g/L (Test 7), the onset of crystallization occurs within the subcooling range of 1.7–13.2 °C. Finally, at a concentration of NaCl to 32 g/L (Test 8), the subcooling range was observed to be much broader between 5.7 °C and 20.9 °C.

3.4 Measurement of crystal growth rate

In this study, the optical microscopy method was used for crystal growth rate measurements. This method is suitable for crystals that are large enough to be visible with the used microscope. The size of the droplets was 850 μm. High-quality Imaging was performed at 25 fps with a 4× microscope zoom to detect the onset and the end of the crystal growth in droplets. Lateral growth of secondary CPH formation was measured at the surface of the water droplet. This method measures the external growing front of the crystals, which is probably not representative of the internal hydrate crystal growth [31]. However as CPH formation requires water and CP and as the CPH crystals are not permeable to CP or water, it can be supposed that the growth is perpendiculat to the interface. As a fast crystallization takes place outside the droplet the growth is probably rapidly stopped inside the droplet due to the lack of one of the constituents (CP or water).

The lateral crystal growth rate evolution is illustrated in Figure 15 for a pure water droplet. The secondary CPH was formed at a subcooling of 4.2 °C, meaning the temperature was decreased from 7.2 °C to 3 °C at a cooling rate of 0.5 °C/min. The microscope was then focused on one droplet and the hydrate growth over time was recorded using a video. The size of the crystals was measured using the image analysis software ImageJ®. The growth rate of the crystals was calculated using the hydrate front measurements and the time intervals between each measurement.

The initial lateral growth occurred at the apex of the water droplet, which exhibited an ascending pattern with

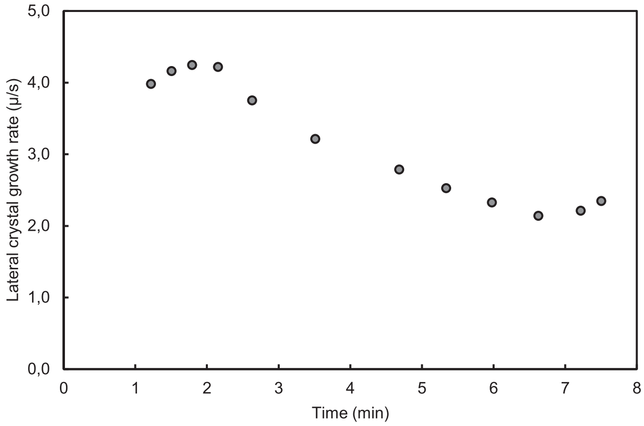

Figure 15. Evolution of the lateral crystal growth rate of secondary CPH formation on the surface of a pure water droplet at a subcooling 4.2 °C.

growth rates ranging from 3.98 µm/s (at 1.2 min), 4.16 µm/s (at 1.5 min), and 4.25 µm/s (at 1.8 min). After this constant increase, a long decrease in the growth rate, ranging from 4.22 µm/s to 2.14 µm/s, is measured between times 2 min and 7 min. Ultimately, a new increase in the growth rate is measured during the last minutes, from 2.21 µm/s to 2.35 µm/s.

It should be noted that hydrate formation induced a change in the size of water droplets from 850 µm to 1057 µm at the end of the crystal formation process at the subcooling of 4.2 °C. Martinez de Baños *et al.* [11] measured lateral growth rates of 2.2 µm/s and 6.7 µm/s, corresponding to a subcooling of 3.1 °C and a subcooling of 7.2 °C, the growth durations of approximately 7 min and 2.5 min, respectively. They observed that the crystal growth rate primarily depends on subcooling. Touil *et al.* [22] investigated velocities in the direction of CP halo growth for various subcooling levels. They reported hydrate growth rates of 1.86 µm/s for a subcooling of 5 °C, 2.82 µm/s and 3.47 µm/s for a subcooling of 5.7 °C and growth rates of 3.59 µm/s and 3.69 µm/s for a subcooling of 6 °C. The findings showcased within this paper demonstrate an average growth rate of 3.2 µm/s for a subcooling of 4.2 °C within a water droplet. The presented results are consistent with the results above [11, 22].

High-quality observation of the crystallization can be achieved through a magnification of 4× (4–6 droplets) or 5× (1–2 droplets) (Fig. 16b). Such observations are essential to study the crystal morphology and determining its lateral growth rate, which will be further discussed in the following section. The microfluidic device facilitates the study of crystal morphology, as depicted in Figure 16c, where CPH crystals can be observed. The image quality presented in this figure confirms the feasibility of studying crystal morphologies. For instance, Sakemoto *et al.* [17] conducted a series of observations on CPH formation at the interface of NaCl aqueous solution to investigate the impact of high salt concentration on CPH crystal growth. The experiment was carried out using a glass test tube measuring 10 mm in external diameter, 8 mm in internal diameter, and 90 mm in height. They explored the correlation between crystal morphology and subcooling in the presence of varying salt concentrations. Our findings indicate that it is feasible to calculate the growth rate and morphology of hydrates as a function of subcooling through high-quality video monitoring using the microfluidic system.

4 Discussion

Compared to the laboratory reactor scale, microfluidic devices offer a higher surface-to-volume ratio and allow also tests' parallelization. In addition, these devices enable to conducting of tests at sizes comparable to porous rock scale. Moreover, a wide choice of geometries is commercially available, and/or "on-demand" geometries can be easily realized with a high degree of accuracy. Additionally, chips working at low temperature and high pressure are available for studies of CO_2 hydrate formation. Using a microfluidic device allows to follow the hydrate formation or dissociation at the droplet level and enables high-resolution imaging of hydrate crystallization. This provides valuable insights into the mechanisms of hydrate nucleation, growth *versus* time, and subcooling. Despite the advantages of microfluidic systems, there are also drawbacks such as channels clogging or fouling by impurities that can reduce the efficiency of the system for hydrate formation tests.

4.1 Ice nucleation

The formation of CPH was initiated by a prior ice formation. The histograms show approximately Gaussian distributions (Fig. 8). These distributions illustrate the stochastic behavior of ice crystallization. The peak distributions as well as the global distributions of the events indicate that the two Tests A1 and A2 with pure water are similar, which confirms the repeatability of the experimental procedure.

The thermodynamic effect of salt was also detected by observing the main conversion peak. The transformed droplets start at the 2nd and 3rd minute for pure water (Fig. 8) and 4th minute for low salt concentration (Test A3, 5 g/L NaCl) and increase to the 5th minute for higher salt concentrations (17.5 and 32 g/L, Tests A4 and A5, respectively, Fig. 9). In conclusion, when salt was added, the patterns remained relatively Gaussian, but the nucleation time and the main conversion peak were delayed.

4.2 Image analysis

The difference between the two images (Fig. 17a and 17b) could be readily observed through visual analysis, characterized by fluctuations in gray pixel intensity. Figure 17a exhibited grayscale shading toward white, while Figure 17b displayed grayscale shading toward black. In addition, the difference observed between the ice state of pure water (Fig. 10b) and salt water (Fig. 17b) was primarily due to the presence of salt. The onset of ice nucleation from Figures 17a to 17b was recorded at a rate of 3000 fps

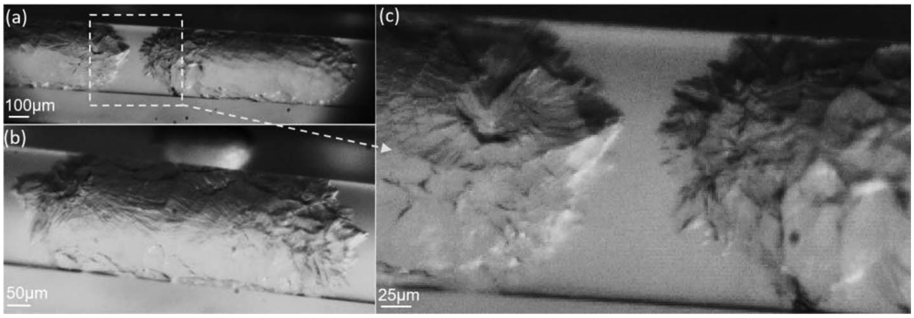

Figure 16. Pictures of CPH morphology using high-quality camera. (a) Displays the distance between two crystallized water droplets, while (c) provides a zoomed-in image of this particular region. Additionally, (b) highlights one of these droplets for further analysis.

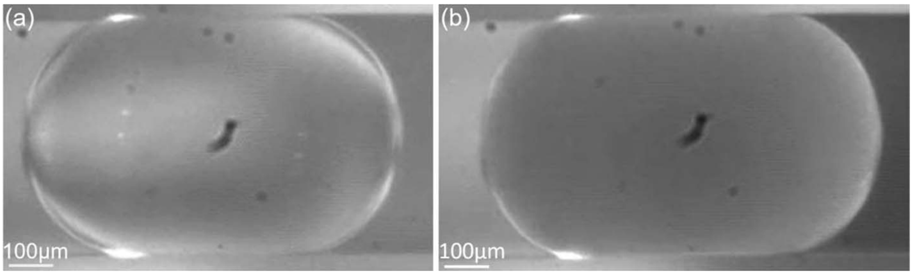

Figure 17. Visualization of the liquid-to-ice phase change in a water droplet: (a) saltwater droplet at 3 °C, (b) ice saltwater droplet at −25 °C.

(frames per second). The video illustrating these observations is available in Supplementary Information Video 2.

4.3 Secondary CPH formation

The effect of T_{dis} and t_{dis} were first assessed in pure water systems. The results showed that T_{dis} had a significant impact on secondary CPH formation. The comparison between Test 1, Test 2, and Test 4 shows that when T_{dis} increased from 7.2 °C to 8.8 °C with $t_{\text{dis}} = 90$ min, the required range of subcooling necessary to form CPH increased from 3.1 °C to 7.2 °C. The fraction of transformed droplets for Test 1, Test 2, and Test 4 reached 100%, 79%, and 66%, respectively. Tests 3 and 4 showed that t_{dis} also influences the CPH formation and the fraction of transformed droplets ($t_{\text{dis}} = 20$ min 100% droplets transformed and $t_{\text{dis}} = 90$ min 66% droplets transformed). These results indicate that the memory effect becomes less prominent for higher melting temperatures and/or longer durations of the melting sequence, consistent with previous observations reported by Martinez de Baños *et al.* [11] and Sefidroodi *et al.* [32].

With saltwater conditions, first, the salt displaces the stability of CPH (as the stability of ice) to lower temperature. NaCl is a thermodynamic inhibitor of hydrates. The presence of salts decreases the equilibrium dissociation temperature. As long as the presence of dissolved salt results in an increase in the interaction of ions with the water molecules that tends to increase the energy required to stabilize hydrates [33].

The experimental findings suggest that the correlation between subcooling and salinity was not uniform among various salinity levels. Notably, Test 5 displayed a significant deviation towards lower subcooling values in comparison to pure water. Additionally, the results from Tests 6 to 7 indicated an inadequate positioning in the diagram when considering the salinity. As the salinity of the droplets increased, there was no logical pattern observed in the diagram. It has been observed that the reproducibility of results is diminished when salt is dissolved within the aqueous phase. This phenomenon may be attributed to potential inhomogeneities in salt concentration within a water droplet, as well as other factors that remain yet to be comprehensively elucidated.

Two hypotheses can be proposed to explain the effect of NaCl, which are listed here:

1. The hydration reaction consumes water molecules and leads to salt exclusion/precipitation, which can increase the local salt-ion concentration and drive the diffusion of salt ions. Besides, as the salt ions concentration can influence guest molecules solubility, the change in the local salt ions concentration also inevitably affects the concentration gradient and the diffusion of guest molecule in brine [30, 34, 35]. Therefore, we can consider that even during the primary CPH formation, the salt concentration is not homogeneous in the droplets, and this phenomenon will be repeated once the formation of the secondary CPH begins;

2. In this condition, the equilibrium dissociation temperature of droplets with high salinity can shift to lower values, causing a reduction in subcooling and a decrease in hydrate growth rate. Conversely, certain droplets may have lower salinity levels during dissociation, leading to higher T_{eq} values [30].

Based on those results, it can be inferred that the formation of secondary CPH in saline water droplets is primarily controlled by the exclusion of NaCl during both primary and secondary CPH formation. The NaCl excluded from the hydrate affects the solution's salinity. However, variations in salinity induced by the experimental procedure can hinder the accurate assessment and study of the effects of high-salinity salts. Similar variations can occur in real reservoir rocks during hydrate formation/dissociation, which may complexify the evaluation of the associated risks due to the unknown minimum salinity of the system. Therefore, precise salinity measurements are necessary to comprehend the behavior of high-salinity systems and the associated hazards of hydrate formation.

5 Conclusions

Experiments on the kinetics of CPH formation were conducted using an in-house droplet-based microfluidic device. The device was able to store trains of identical water droplets, and was equipped with a high-quality optical observation platform; this system allows precise control of the conditions at which hydrate formation takes place, such as temperature and fluid composition. Additionally, the small size of microfluidic channels allows the application of rapid heating/cooling cycles and good mass transfer, which can accelerate hydrate formation and improve the efficiency of the process. The procedure consisted of three crystallizations (ice then two CPH formations). First, ice was formed and then melted by heating. This melting initiated the first CPH formation. Finally, the temperature was increased up to above T_{eq} to melt the CPH and then lowered to below T_{eq} to initiate the secondary CPH formation by the memory effect.

CPH formations in pure water and salt water exhibit differences due to the influence of the salt (NaCl) on thermodynamic equilibrium and on kinetics. In pure water, hydrate formation was mainly influenced by temperature, and the absence of other dissolved ions (salts) in water allowed repeatable and logical results. This study represented the initial endeavor to investigate the impact of NaCl on CPH formation at the microfluidic scale for isolated water droplets. The presence of NaCl in water in the procedure used had a significant impact on the ice and CPH formations. The results did not follow the same pattern when NaCl concentration was changed. Furthermore, the observed results do not exhibit a consistent trend *versus* NaCl concentrations. This study provides important insights into the complex role of salts in the CPH formation probably because of the concentration variations/precipitation of salt in the droplets when the procedure is applied. The kinetics of clathrate hydrate formation, specifically nucleation and growth, are influenced by several parameters. This study aimed to investigating the impact of subcooling and the presence of salt (NaCl) on the CPH formation. Our results indicate that increasing subcooling leads to faster nucleation and a higher growth rate. Conversely, the concentration of salt had an inhibiting effect on nucleation and growth. Increasing salt concentration leads to slower nucleation and growth rates due to the change in the equilibrium stability of the CPH and consequently to the subcooling's decrease imposed on the systems.

In conclusion, repeatable and comparable results require constant and homogeneous NaCl concentration in all the water droplets from the beginning till the end of a test. The procedure must be adapted in order to avoid these salt variations. Subsequent research efforts could replicate this study utilizing Raman microscopy to explore and study the water droplets during hydrate formation. This work will be continued and will focus on the study of CO_2 hydrate formation using microfluidic devices. It will allow a deeper understanding of hydrate formation in the presence of salt. It will provide knowledge and data for carbon storage in porous rocks in depleted hydrocarbon reservoirs, deep saline aquifers, or unconventional reservoirs such as coal seams or basalts.

Supplementary Information

The supplementary information of this article is available at https://stet-review.org/10.2516/stet/2023034/olm.
Supplementary Information Video 1: An overview of serpentine tubes and the generation of uniform and isolated water droplets.
Supplementary Information Video 2: The onset of ice nucleation at a frame rate of 3000 fps.

References

1 IEA – International Energy Agency (2016) *20 years of carbon capture and storage – accelerating future deployment*, OECD/IEA.

2 Rayward-Smith W.J., Woods A.W. (2011) Some implications of cold CO_2 injection into deep saline aquifers, *Geophys. Res. Lett.* **38**, 6, n/a–n/a. https://doi.org/10.1029/2010GL046412.

3 Vilarrasa V., Silva O., Carrera J., *et al.* (2013) Liquid CO_2 injection for geological storage in deep saline aquifers, *Int. J. Greenh. Gas Control* **14**, 84–96. https://doi.org/10.1016/j.ijggc.2013.01.015.

4 Hoteit H., Fahs M., Soltanian M.R. (2019) Assessment of CO_2 injectivity during sequestration in depleted gas reservoirs, *Geosciences* **9**, 5, 199. https://doi.org/10.3390/geosciences9050199.

5 Oldenburg C.M. (2007) Joule–Thomson cooling due to CO_2 injection into natural gas reservoirs, *Energy Convers. Manag.* **48**, 6, 1808–1815. https://doi.org/10.1016/j.enconman.2007.01.010.

6 Gao M., Wang L., Chen X., *et al.* (2021) Joule–Thomson effect on a CCS-relevant ($CO_2 + N_2$) system, *ACS Omega* **6**, 14, 9857–9867. https://doi.org/10.1021/acsomega.1c00554.

7 Sloan E.D. Jr., Koh C.A. (2008) *Clathrate hydrates of natural gases*, 3rd ed., CRC Press, Boca Raton. https://doi.org/10.1201/9781420008494.

8 Ho-Van S., Douzet J., Le-Quang D., Bouillot B., Herri J.M. (2016) Behavior of cyclopentane hydrates formation and dissociation in pure water and in the presence of sodium chloride, in: International Conferences On Earth Sciences And Sustainable Georesources Development-ESASGD, Hanoï, Vietnam. pp. 150–157. https://hal.science/hal-01466636.

9 Sun S., Peng X., Zhang Y., *et al.* (2017) Stochastic nature of nucleation and growth kinetics of THF hydrate, *J. Chem. Thermodyn.* **107**, 141–152. https://doi.org/10.1016/j.jct.2016.12.026.

10 Zeng H., Wilson L.D., Walker V.K., *et al.* (2006) Effect of antifreeze proteins on the nucleation, growth, and the memory effect during tetrahydrofuran clathrate hydrate formation, *J. Am. Chem. Soc.* **128**, 9, 2844–2850. https://doi.org/10.1021/ja0548182.

11 Martinez de Baños M.L., Carrier O., Bouriat P., *et al.* (2015) Droplet-based millifluidics as a new tool to investigate hydrate crystallization: insights into the memory effect, *Chem. Eng. Sci.* **123**, 564–572. https://doi.org/10.1016/j.ces.2014.11.018.

12 Ho-Van S., Bouillot B., Garcia D., *et al.* (2019) Crystallization mechanisms and rates of cyclopentane hydrates formation in brine, *Chem. Eng. Technol.* **42**, 7, 1481–1491. https://doi.org/10.1002/ceat.201800746.

13 Maghsoodloo Babakhani S., Ho-Van S., Bouillot B., *et al.* (2020) Phase equilibrium measurements and modelling of mixed cyclopentane and carbon dioxide hydrates in presence of salts, *Chem. Eng. Sci.* **214**, 115442–115453. https://doi.org/10.1016/j.ces.2019.115442.

14 Zylyftari G., Ahuja A., Morris J.F. (2014) Nucleation of cyclopentane hydrate by ice studied by morphology and rheology, *Chem. Eng. Sci.* **116**, 497–507. https://doi.org/10.1016/j.ces.2014.05.019.

15 Sakemoto R., Sakamoto H., Shiraiwa K., *et al.* (2010) Clathrate hydrate crystal growth at the seawater/hydrophobic−guest−liquid interface, *Cryst. Growth Des.* **10**, 3, 1296–1300. https://doi.org/10.1021/cg901334z.

16 Li X., Wang C., Liang S., *et al.* (2020) Experimental visualization of cyclopentane hydrate dissociation behavior in a microfluidic chip, *Chem. Eng. Sci.* **227**, 115937. https://doi.org/10.1016/j.ces.2020.115937.

17 Zhao C.-X., Middelberg A.P. (2011) Two-phase microfluidic flows, *Chem. Eng. Sci.* **66**, 7, 1394–1411. https://doi.org/10.1016/j.ces.2010.08.038.

18 Utada A.S., Fernandez-Nieves A., Stone H.A., *et al.* (2007) Dripping to jetting transitions in coflowing liquid streams, *Phys. Rev. Lett.* **99**, 9, 94502. https://doi.org/10.1103/PhysRevLett.99.094502.

19 Atig D., Touil A., Ildefonso M., *et al.* (2018) A droplet-based millifluidic method for studying ice and gas hydrate nucleation, *Chem. Eng. Sci.* **192**, 1189–1197. https://doi.org/10.1016/j.ces.2018.08.003.

20 Touil A., Broseta D., Desmedt A. (2019) Gas hydrate crystallization in thin glass capillaries: roles of supercooling and wettability, *Langmuir* **35**, 38, 12569–12581. https://doi.org/10.1021/acs.langmuir.9b01146.

21 Cai L., Pethica B.A., Debenedetti P.G., *et al.* (2016) Formation of cyclopentane methane binary clathrate hydrate in brine solutions, *Chem. Eng. Sci.* **141**, 125–132. https://doi.org/10.1016/j.ces.2015.11.001.

22 Touil A., Broseta D., Hobeika N., *et al.* (2017) Roles of wettability and supercooling in the spreading of cyclopentane hydrate over a substrate, *Langmuir* **33**, 41, 10965–10977. https://doi.org/10.1021/acs.langmuir.7b02121.

23 Miralles V., Huerre A., Malloggi F., *et al.* (2013) A review of heating and temperature control in microfluidic systems: techniques and applications, *Diagnostics* **3**, 1, 33–67. https://doi.org/10.3390/diagnostics3010033.

24 Davaj B. (2016) Thermal microfluidic devices; design, fabrication and applications, *PhD Thesis*, Marquette University, 33 p.

25 Stan C.A., Schneider G.F., Shevkoplyas S.S., *et al.* (2009) A microfluidic apparatus for the study of ice nucleation in supercooled water drops, *Lab Chip* **9**, 16, 2293–2305. https://doi.org/10.1039/b906198c.

26 Teychené S., Biscans B. (2012) Crystal nucleation in a droplet based microfluidic crystallizer, *Chem. Eng. Sci.* **77**, 242–248. https://doi.org/10.1016/j.ces.2012.01.036.

27 Teychené S., Biscans B. (2011) Microfluidic device for the crystallization of organic molecules in organic solvents, *Cryst. Growth Des.* **11**, 11, 4810–4818. https://doi.org/10.1021/cg2004535.

28 Radajewski D. (2017) Etudes de nucléation de protéines à l'aide de dispositifs expérimentaux microfludiques, *PhD Thesis*, Toulouse University, 27 p.

29 Ho-Van S., Bouillot B., Douzet J., *et al.* (2018) Experimental measurement and thermodynamic modeling of cyclopentane hydrates with NaCl, KCl, $CaCl_2$, or NaCl-KCl present, *AIChE J.* **64**, 6, 2207–2218. https://doi.org/10.1002/aic.16067.

30 Kishimoto M., Iijima S., Ohmura R. (2012) Crystal growth of clathrate hydrate at the interface between seawater and hydrophobic-guest liquid: effect of elevated salt concentration, *Ind. Eng. Chem. Res.* **51**, 14, 5224–5229. https://doi.org/10.1021/ie202785z.

31 Sun C.Y., Peng B.Z., Dandekar A., *et al.* (2010) Studies on hydrate film growth, *Annu. Rep. Prog. Chem., Sect. C: Phys. Chem.* **106**, 77. https://doi.org/10.1039/b811053k.

32 Sefidroodi H., Abrahamsen E., Kelland M.A. (2013) Investigation into the strength and source of the memory effect for cyclopentane hydrate, *Chem. Eng. Sci.* **87**, 133–140. https://doi.org/10.1016/j.ces.2012.10.018.

33 Zylyftari G., Lee J.W., Morris J.F. (2013) Salt effects on thermodynamic and rheological properties of hydrate forming emulsions, *Chem. Eng. Sci.* **95**, 148–160. https://doi.org/10.1016/j.ces.2013.02.056.

34 Qi Y., Wu W., Liu Y., *et al.* (2012) The influence of NaCl ions on hydrate structure and thermodynamic equilibrium conditions of gas hydrates, *Fluid Phase Equilib.* **325**, 6–10. https://doi.org/10.1016/j.fluid.2012.04.009.

35 Lv Y.-N., Wang S.-S., Sun C.-Y., *et al.* (2017) Desalination by forming hydrate from brine in cyclopentane dispersion system, *Desalination* **413**, 217–222. https://doi.org/10.1016/j.desal.2017.03.025.